

Ionized calcium in the atmospheres of two ultra-hot exoplanets WASP-33b and KELT-9b[★]

F. Yan (✉)¹, N. Casasayas-Barris^{2,3}, K. Molaverdikhani⁴, F. J. Alonso-Floriano⁵, A. Reiners¹, E. Pallé^{2,3}, Th. Henning⁴, P. Mollière⁵, G. Chen⁶, L. Nortmann^{2,3}, I. A. G. Snellen⁵, I. Ribas^{7,8}, A. Quirrenbach⁹, J. A. Caballero¹⁰, P. J. Amado¹¹, M. Azzaro¹², F. F. Bauer¹¹, M. Cortés Contreras¹⁰, S. Czesla¹³, S. Khalafinejad⁹, L. M. Lara¹¹, M. López-Puertas¹¹, D. Montes¹⁴, E. Nagel¹³, M. Oshagh¹, A. Sánchez-López¹¹, M. Stangret^{2,3}, and M. Zechmeister¹

¹ Institut für Astrophysik, Georg-August-Universität, Friedrich-Hund-Platz 1, 37077 Göttingen, Germany
e-mail: fei.yan@uni-goettingen.de

² Instituto de Astrofísica de Canarias (IAC), Calle Vía Lactea s/n, 38200 La Laguna, Tenerife, Spain

³ Departamento de Astrofísica, Universidad de La Laguna, 38026 La Laguna, Tenerife, Spain

⁴ Max-Planck-Institut für Astronomie, Königstuhl 17, 69117 Heidelberg, Germany

⁵ Leiden Observatory, Leiden University, Postbus 9513, 2300 RA Leiden, The Netherlands

⁶ Key Laboratory of Planetary Sciences, Purple Mountain Observatory, Chinese Academy of Sciences, Nanjing 210033, PR China

⁷ Institut de Ciències de l'Espai (CSIC-IEEC), Campus UAB, c/ de Can Magrans s/n, 08193 Bellaterra, Barcelona, Spain

⁸ Institut d'Estudis Espacials de Catalunya (IEEC), 08034 Barcelona, Spain

⁹ Landessternwarte, Zentrum für Astronomie der Universität Heidelberg, Königstuhl 12, 69117 Heidelberg, Germany

¹⁰ Centro de Astrobiología (CSIC-INTA), ESAC, Camino bajo del castillo s/n, 28692 Villanueva de la Cañada, Madrid, Spain

¹¹ Instituto de Astrofísica de Andalucía (IAA-CSIC), Glorieta de la Astronomía s/n, 18008 Granada, Spain

¹² Centro Astronómico Hispano-Alemán (CSIC-MPG), Observatorio Astronómico de Calar Alto, Sierra de los Filabres, 04550 Gérgal, Almería, Spain

¹³ Hamburger Sternwarte, Universität Hamburg, Gojenbergsweg 112, 21029 Hamburg, Germany

¹⁴ Departamento de Física de la Tierra y Astrofísica and IPARCOS-UCM (Instituto de Física de Partículas y del Cosmos de la UCM), Facultad de Ciencias Físicas, Universidad Complutense de Madrid, 28040 Madrid, Spain

Received 28 July 2019 / Accepted 30 October 2019

ABSTRACT

Ultra-hot Jupiters are emerging as a new class of exoplanets. Studying their chemical compositions and temperature structures will improve our understanding of their mass loss rate as well as their formation and evolution. We present the detection of ionized calcium in the two hottest giant exoplanets – KELT-9b and WASP-33b. By using transit datasets from CARMENES and HARPS-N observations, we achieved high-confidence-level detections of Ca II using the cross-correlation method. We further obtain the transmission spectra around the individual lines of the Ca II H&K doublet and the near-infrared triplet, and measure their line profiles. The Ca II H&K lines have an average line depth of $2.02 \pm 0.17\%$ (effective radius of $1.56 R_p$) for WASP-33b and an average line depth of $0.78 \pm 0.04\%$ (effective radius of $1.47 R_p$) for KELT-9b, which indicates that the absorptions are from very high upper-atmosphere layers close to the planetary Roche lobes. The observed Ca II lines are significantly deeper than the predicted values from the hydrostatic models. Such a discrepancy is probably a result of hydrodynamic outflow that transports a significant amount of Ca II into the upper atmosphere. The prominent Ca II detection with the lack of significant Ca I detection implies that calcium is mostly ionized in the upper atmospheres of the two planets.

Key words. planets and satellites: atmospheres – techniques: spectroscopic – planets and satellites: individual: WASP-33b – planets and satellites: individual: KELT-9b

1. Introduction

Ultra-hot Jupiters (UHJs) are a recently discovered class of exoplanets. They are highly irradiated gas giants with day-side temperatures that are typically $\gtrsim 2200$ K (Parmentier et al. 2018). Most of these planets orbit very close to A- or F-type stars. Their extremely high day-side temperatures cause thermal dissociation of molecules and ionization of atoms (Arcangeli et al. 2018; Lothringer et al. 2018). Depending on the heat transport efficiency, different chemical components can form at their

night-sides as well as terminators (Parmentier et al. 2018; Bell & Cowan 2018; Helling et al. 2019). Furthermore, the strong stellar ultraviolet (UV) and/or extreme-UV irradiation causes significant mass loss, affecting the planetary atmospheric composition and evolution (Bisikalo et al. 2013; Fossati et al. 2018).

Observations of UHJs have revealed peculiar properties of their atmospheres. For example, Kreidberg et al. (2018) found the absence of H₂O features at the day-side atmosphere of WASP-103b and these latter authors attributed this to the thermal dissociation of H₂O. Arcangeli et al. (2018) analyzed the day-side spectrum of WASP-18b and found that molecules are thermally dissociated while the H⁻ ion opacity becomes important. Yan & Henning (2018) detected strong hydrogen H α absorption in the

[★] The reduced transmission spectrum is only available at the CDS via anonymous ftp to cdsarc.u-strasbg.fr (130.79.128.5) or via <http://cdsarc.u-strasbg.fr/viz-bin/cat/J/A+A/632/A69>

transmission spectrum of KELT-9b, which indicates that the planet has a hot escaping hydrogen atmosphere. The $H\alpha$ line was also detected in two other UHJs: MASCARA-2b (Casasayas-Barris et al. 2018) and WASP-12b (Jensen et al. 2018). Some atomic and ionic metal lines are also detected in UHJs, for instance, Fossati et al. (2010) detected Mg II in WASP-12b using UV transmission spectroscopy with the *Hubble* Space Telescope and various metal elements (including Fe, Ti, Mg, and Na) have been discovered in KELT-9b (Hoeijmakers et al. 2018, 2019; Cauley et al. 2019).

Theoretically, calcium should exist and probably becomes ionized into Ca II in the upper atmosphere of UHJs. Khalafinejad et al. (2018) analyzed the Ca II near-infrared triplet during the transit of the hot gas giant WASP-17b but did not detect any Ca II signals. Very recently, the Ca II near infrared triplet lines were detected for the first time in MASCARA-2b, an UHJ with equilibrium temperature $T_{\text{eq}} \sim 2260$ K (Casasayas-Barris et al. 2019). Ca II can also exist in the exospheres of rocky planets (Mura et al. 2011). For example, Ca II is detected in the exosphere of Mercury (Vervack et al. 2010). Ridden-Harper et al. (2016) searched for Ca II in the exosphere of the hot rocky planet 55 Cancri e and they found a tentative signal of Ca II in one of the four transit datasets. Guenther et al. (2011) attempted to detect calcium in the exosphere of another hot rocky planet, Corot-7b, but were only able to derive an upper limit of the amount of calcium in the exosphere.

Here we report the detections of Ca II in two UHJs: KELT-9b and WASP-33b. KELT-9b ($T_{\text{eq}} \sim 4050$ K) is the hottest exoplanet discovered so far (Gaudi et al. 2017) and its host star is a fast-rotating early A-type star. Hydrogen Balmer lines and several kinds of metals (Yan & Henning 2018; Hoeijmakers et al. 2018; Cauley et al. 2019), but not Ca II, have been detected in its atmosphere. WASP-33b ($T_{\text{eq}} \sim 2710$ K) is the second hottest giant exoplanet, and orbits a fast-rotating A5-type star (Collier Cameron et al. 2010). The host star is a δ Scuti variable (Herrero et al. 2011; von Essen et al. 2014). A temperature inversion, as well as TiO and evidence of AlO, have been detected in the planet (Haynes et al. 2015; Nugroho et al. 2017; von Essen et al. 2019).

The paper is organized as follows. We present transit observations of the above two planets in Sect. 2. In Sect. 3, we describe the method used to obtain the transmission spectrum of the five Ca II lines – the two H&K doublet lines and the three near-infrared triplet (IRT) lines. In Sect. 4, we present the results and discussions including the cross-correlation signal, transmission spectra of individual Ca II lines, mixing ratios of Ca I and Ca II, and comparison with models. Conclusions are presented in Sect. 5.

2. Observations

For each of the two planets, we analyzed one transit dataset from CARMENES covering the Ca II IRT lines and one transit dataset from HARPS-North (HARPS-N) covering the Ca II H&K lines.

2.1. WASP-33b observations

We observed two transits of WASP-33b. The first transit was observed on 5 January 2017 with the CARMENES (Quirrenbach et al. 2018) spectrograph, installed at the 3.5 m telescope of the Calar Alto Observatory. The CARMENES visual channel has a high spectral resolution ($R \sim 94\,600$) and a wide spectral coverage (520–960 nm). A continuous observing sequence of ~ 4.5 h was performed, covering 0.7 h before transit and 0.8 h

after transit. The exposure time was set to 120 s, but the first 19 spectra had shorter exposure times (ranging from 65 to 120 s). The data reduction of the raw spectra was performed with the CARACAL pipeline (Caballero et al. 2016), which includes bias, flatfield, and cosmic ray corrections, and wavelength calibration. The spectrum produced by the pipeline is at vacuum wavelength and in the Earth’s rest frame. We converted the wavelengths into air wavelengths in our study.

The second transit was observed on 8 November 2018 with the HARPS-N spectrograph mounted on the Telescopio Nazionale *Galileo*. The instrument has a resolution of $R \sim 115\,000$ and a wavelength coverage of 383–690 nm. The observation lasted for 9 h, and we obtained 141 spectra. The raw data were reduced with the HARPS-N pipeline (Data Reduction Software). The pipeline produces order-merged, one-dimensional spectra with a re-sampled wavelength step of 0.01 Å. The barycentric Earth radial velocity (RV) was already corrected by the pipeline, but we converted it back into the Earth’s rest frame in order to be consistent with the CARMENES data. The observation logs of the two transits are summarized in Table 1.

2.2. KELT-9b observations

We used archival data of one transit from CARMENES observations and one transit from HARPS-N observations. The details of the two observations were described in Yan & Henning (2018) and Hoeijmakers et al. (2018), respectively (see Table 1 for summaries). The CARMENES observation was performed under partially cloudy weather conditions, and therefore the spectral signal-to-noise ratio (S/N) was relatively low, and part of the observation was lost due to clouds passing by.

3. Method

We used two different methods to search for and study the Ca II lines: the cross-correlation method and the direct transmission spectrum of individual lines. The cross-correlation of high-resolution spectroscopic observations with theoretical model spectra has proven to be a powerful and robust technique to detect molecular and atomic species in exoplanet atmospheres (e.g., Snellen et al. 2010; Alonso-Floriano et al. 2019). The direct transmission spectrum method allows detailed study of the line profiles and direct comparison with models (e.g., Wyttenbach et al. 2015; Yan & Henning 2018). In this work, we focused on the Ca II H&K lines (K line 3933.66 Å, H line 3968.47 Å) and the Ca II IRT lines (8498.02 Å, 8542.09 Å, 8662.14 Å). These five lines are the strongest Ca II lines in the observed wavelength range.

3.1. Obtaining the transmission spectral matrix

The transmission spectrum of each Ca II line was retrieved separately. We firstly normalized the spectrum and then removed the telluric and stellar lines. The telluric removal was performed in the Earth’s rest frame. The telluric lines in the wavelength range of the Ca II lines are mostly H₂O lines. We employed a theoretical H₂O transmission model described in Yan et al. (2015b). The model was used to fit and remove the H₂O lines (Fig. 1). The removal of the stellar lines was performed by dividing each spectrum by the out-of-transit master spectrum. The master spectrum was obtained by averaging all the observed out-of-transit spectra with their continuum S/N as weights. Before obtaining the master spectrum, we aligned all the spectra to the stellar rest frame by correcting the barycentric Earth RV and systemic velocity

Table 1. Observation log.

	Instrument	Wavelength coverage	Date	Exposure time [s]	N_{spectra}
WASP-33b	CARMENES	520–960 nm (contains IRT lines)	2017-01-05	120 ^(a)	93
	HARPS-N	383–690 nm (contains H&K lines)	2018-11-08	200	141
KELT-9b	CARMENES	520–960 nm (contains IRT lines)	2017-08-06	300, 400	48
	HARPS-N	383–690 nm (contains H&K lines)	2017-07-31	600	49

Notes. ^(a)The first 19 spectra had exposure times shorter than 120 s.

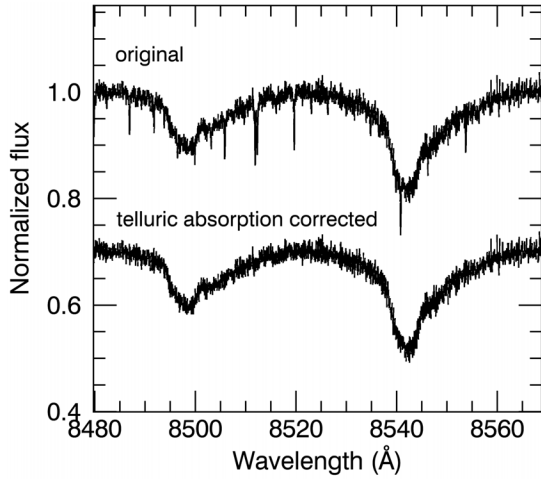


Fig. 1. Example of telluric removal. The upper line is the normalized spectrum around two of the Ca II IRT lines of KELT-9. The lower line is the telluric absorption corrected spectrum (shifted down by 0.3 for clarity).

(-3.0 km s^{-1} for WASP-33b and -20.6 km s^{-1} for KELT-9b). By performing such a division, the residual spectra during transit should contain the transmission signal from the planetary atmosphere, while the spectra out-of-transit should be normalized to unity.

3.2. Correction of stellar RM and CLV effects

During the exoplanet transit, the stellar line profile changes due to the Rossiter-McLaughlin (RM) effect and the center-to-limb variation (CLV) effect. The RM effect (Rossiter 1924; McLaughlin 1924; Queloz et al. 2000) causes line profile distortions due to stellar rotation. The CLV effect is the variation of stellar lines across the center of the stellar disk to the limb (Yan et al. 2015a; Czesla et al. 2015; Yan et al. 2017), and the effect is mostly the result of differential limb darkening between the stellar line and the adjacent continuum.

These two effects are encoded in the obtained transmission spectral matrix and the strength of these effects depends on the actual stellar and planetary parameters. The evaluation and correction of the RM and CLV effects are required for transmission spectrum studies. The effects of different lines and different planets have been evaluated, for example, by Casasayas-Barris et al. (2018), Yan & Henning (2018), Salz et al. (2018), Nortmann et al. (2018), and Keles et al. (2019).

We modeled and corrected the RM and CLV effects simultaneously following the method in Yan & Henning (2018). The details of the CLV-only model are described in Yan et al. (2017) and we included the RM effect by assigning the rotational

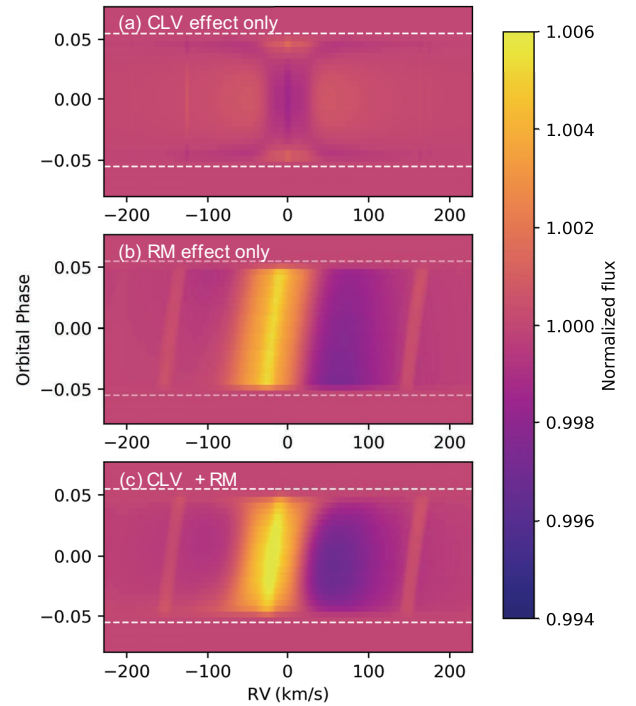


Fig. 2. Models of separate CLV and RM effects of the Ca II K 3933.66 Å line for KELT-9b. The upper panel is the CLV effect-only model, the middle panel is the RM effect-only model, and the bottom panel is the model combining both effects. For fast rotating stars like KELT-9, the RM effect is stronger than the CLV effect. The simulation here is for the $1 R_p$ case.

RV to each of the stellar surface elements as done in Yan & Henning (2018). The RM effect is generally stronger than the CLV effect for these fast rotating stars (cf. Fig. 2 for RM-only and CLV-only models). The correction of the RM effect is a crucial step in performing the transmission spectroscopy of UHJs because their host stars are normally early-type stars that are fast rotators. The stellar and planetary parameters used for the systems of WASP-33b and KELT-9b are listed in Tables 2 and 3, respectively.

The planetary orbit of WASP-33b undergoes a nodal precession as discovered by Johnson et al. (2015). These latter authors measured the changes of orbital inclination and the spin-orbit misalignment angle at two different epochs (2008 and 2014) using Doppler tomography. Measuring the current spin-orbit misalignment during our observations would require additional data reduction procedures such as filtering the stellar pulsation (Johnson et al. 2015), which is beyond the scope of this paper. Therefore, we adopted the change rates and calculated the expected orbital inclination and spin-orbit angle at the dates of our observations.

Table 2. Parameters of the WASP-33b system.

Parameter	Symbol [unit]	Value
<i>The star</i>		
Effective temperature	T_{eff} [K]	7430 ± 100 ^(a)
Radius	R_{\star} [R_{\odot}]	$1.509^{+0.016}_{-0.027}$ ^(a)
Mass	M_{\star} [M_{\odot}]	$1.561^{+0.045}_{-0.079}$ ^(a)
Metallicity	[Fe/H] [dex]	-0.1 ± 0.2 ^(a)
Rotational velocity	$v \sin i_{\star}$ [km s^{-1}]	$86.63^{+0.37}_{-0.32}$ ^(b)
Systemic velocity	v_{sys} [km s^{-1}]	-3.0 ± 0.4 ^(c)
<i>The planet</i>		
Radius	R_{p} [R_{J}]	$1.679^{+0.019}_{-0.030}$ ^(a)
Mass	M_{p} [M_{J}]	2.16 ± 0.20 ^(a)
Orbital semi-major axis	a [R_{\star}]	3.69 ± 0.05 ^(a)
Orbital period	P [d]	1.219870897 ^(d)
Transit epoch (BJD)	T_0 [d]	$2\,454\,163.22449$ ^(d)
Transit depth	δ [%]	1.4 ^(a)
RV semi-amplitude	K_{p} [km s^{-1}]	231 ± 3 ^(a)
Equilibrium temperature	T_{eq} [K]	2710 ± 50
<i>2017 January 5</i>		
Orbital inclination	i [deg]	89.50 ^(e)
Spin-orbit inclination	λ [deg]	-114.05 ^(e)
<i>2018 November 8</i>		
Orbital inclination	i [deg]	90.14 ^(e)
Spin-orbit inclination	λ [deg]	-114.93 ^(e)

References. ^(a)Adopted from Lehmann et al. (2015) with parameters from Kovács et al. (2013). ^(b)Adopted from Johnson et al. (2015). ^(c)Adopted from Nugroho et al. (2017). ^(d)Adopted from Maciejewski et al. (2018). ^(e)Predicted value using parameters in Johnson et al. (2015).

Table 3. Parameters of the KELT-9b system.

Parameter	Symbol [unit]	Value ^(a)
<i>The star</i>		
Effective temperature	T_{eff} [K]	$10\,170 \pm 450$
Radius	R_{\star} [R_{\odot}]	$2.362^{+0.075}_{-0.063}$
Mass	M_{\star} [M_{\odot}]	$2.52^{+0.25}_{-0.20}$
Metallicity	[Fe/H] [dex]	-0.03 ± 0.2
Rotational velocity	$v \sin i_{\star}$ [km s^{-1}]	111.4 ± 1.3
Systemic velocity	v_{sys} [km s^{-1}]	-20.6 ± 0.1
<i>The planet</i>		
Radius	R_{p} [R_{J}]	$1.891^{+0.061}_{-0.053}$
Mass	M_{p} [M_{J}]	2.88 ± 0.84
Orbital semi-major axis	a [R_{\star}]	3.15 ± 0.09
Orbital period	P [d]	1.4811235
Transit epoch (BJD)	T_0 [d]	$2\,457\,095.68572$
Transit depth	δ [%]	0.68
RV semi-amplitude	K_{p} [km s^{-1}]	254^{+12}_{-10}
Equilibrium temperature	T_{eq} [K]	4050 ± 180
Orbital inclination	i [deg]	86.79 ± 0.25
Spin-orbit inclination	λ [deg]	-84.8 ± 1.4

Notes. ^(a)All the parameters are adopted from Gaudi et al. (2017).

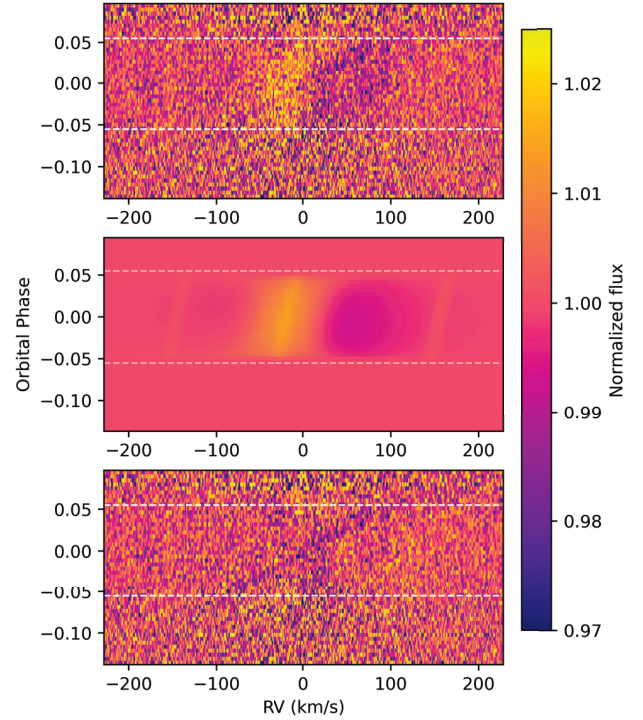


Fig. 3. RM + CLV effects of the Ca II K 3933.66 Å line for KELT-9b. *Upper panel:* observed transmission spectral matrix. *Middle panel:* simulated stellar line profile changes due to the RM + CLV effects with an f factor $f = 2.1$ (see text). Separate models of the CLV effect and RM effect are presented in Fig. 2. *Bottom panel:* transmission spectrum after the correction of the RM + CLV effects. The white horizontal lines label ingress and egress. The obvious shadow with a RV drift from -90 km s^{-1} at ingress to $+90 \text{ km s}^{-1}$ at egress is the planetary absorption.

As noted by Yan & Henning (2018), the actual effective radius at a given spectral line is larger than $1 R_{\text{p}}$ because of the planetary atmospheric absorption. Consequently, the model of the RM + CLV effects should be built with a larger effective radius. We introduced a factor f to account for such an effect by assuming that the actual stellar line profile change is f times the simulated RM + CLV effects with $1 R_{\text{p}}$. In addition, our model has intrinsic errors. For example, our model is in 1D local thermodynamic equilibrium (LTE), while the actual stellar profile is better characterized by a 3D nonLTE stellar model. Thus, such an f factor can also account for the errors of the model. By fitting the observed line profile change with the models using a Markov chain Monte Carlo analysis (Foreman-Mackey et al. 2013), we obtained $f = 2.1 \pm 0.1$ for the Ca II K line and $f = 1.6 \pm 0.2$ for the Ca II H line. For all the other lines, we simply used the $1 R_{\text{p}}$ scenario as the data are not of sufficient quality to obtain an f value.

Figure 3 presents the model result of the Ca II 3933.66 Å line of KELT-9b as an example. The stellar RM and CLV effects dominate the line profile change. After correcting these stellar effects, we were able to detect the planetary absorption clearly. The effects of the Ca II lines behave differently from the effects of the H α line (supplementary Fig. 2 in Yan & Henning 2018), demonstrating the importance of modeling the RM and CLV effects for individual lines.

3.3. Cross-correlation with simulated template

We simulated the Ca II transmission spectra using the *petitRADTRANS* code (Mollière et al. 2019). We assumed that

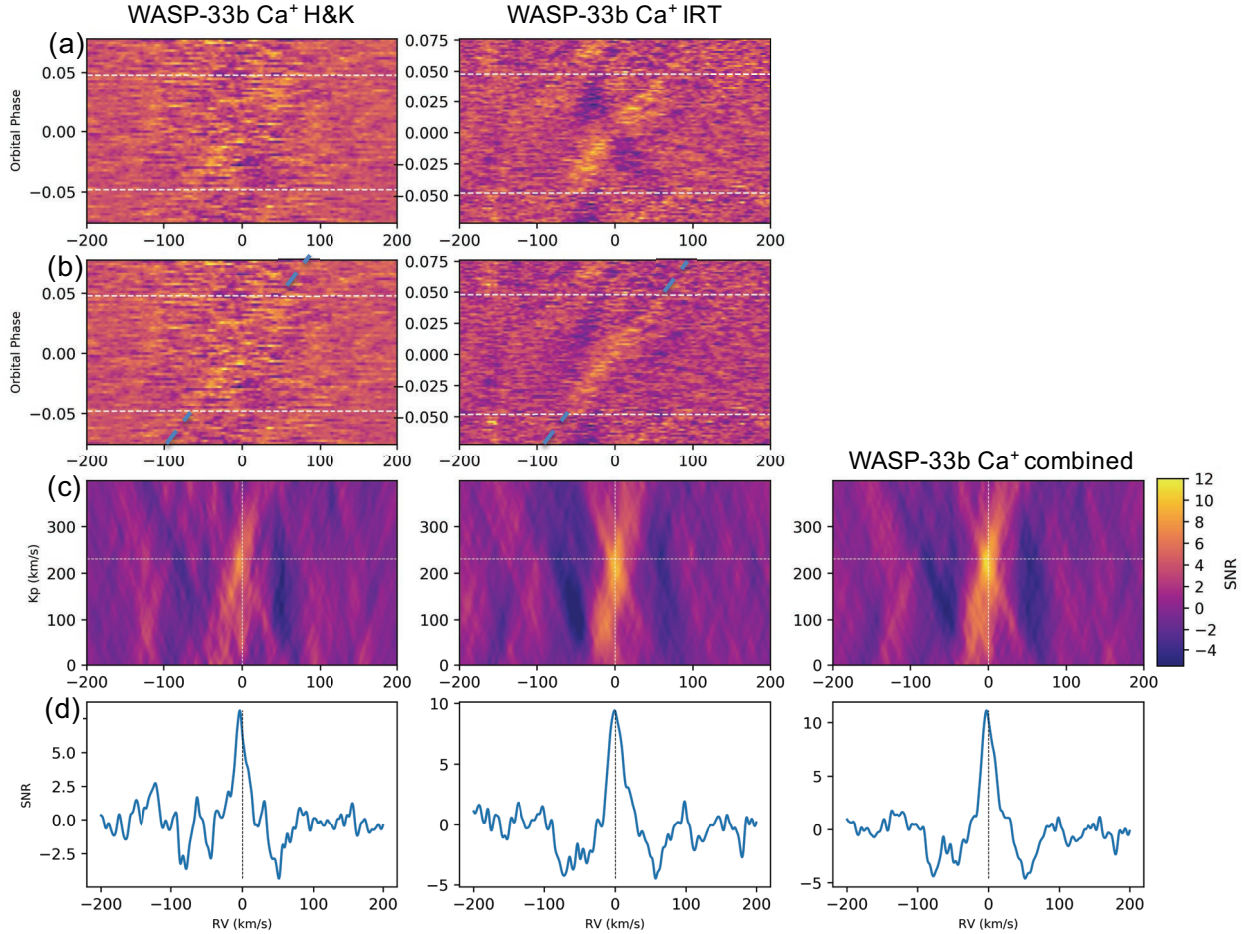


Fig. 4. Cross-correlation results of WASP-33b for Ca II H&K (*left panels*), Ca II IRT (*middle panels*), and the five lines combined (*right panels*). (*a*) The CCF maps without the correction of stellar effects. The two horizontal dashed lines indicate the time of ingress and egress. (*b*) The CCF maps with stellar RM+CLV effects corrected. The correction of RM+CLV effects was performed on the transmission spectral matrix before the cross-correlation. There is a remaining black stripe at -30 km s^{-1} in the CCF map of Ca II IRT, which is probably the feature of stellar pulsation because WASP-33 is a variable star. (*c*) The K_p -map. These are the combined in-transit CCFs for different K_p values. The horizontal dashed line marks the expected K_p calculated using the planetary orbital parameters from the literature. The vertical dashed line marks $\text{RV} = 0 \text{ km s}^{-1}$, where the planetary signal is expected to be located (we corrected the stellar systemic RV). (*d*) The CCF at $K_p = 231 \text{ km s}^{-1}$ (expected K_p value).

the atmosphere has a solar abundance and an isothermal temperature with a value close to the equilibrium temperature (2700 K for WASP-33b and 4000 K for KELT-9b). We also assumed that Ca I is completely ionized into Ca II. We used a mean molecular weight of 1.3 which is the value for an atomic atmosphere with solar abundance. According to Hoeijmakers et al. (2019), the transmission spectral continuum due to H^- absorption in UHJs is normally between 1 and 10 mbar, and the atmosphere below the continuum level cannot be probed. Thus, we set a continuum level of 1 mbar when simulating the transmission spectrum. This was done by adding an absorber of infinite strength for $P > 1$ mbar. The template spectra were subsequently convolved with the instrument profiles. We established a grid of template spectra with RV shifts from -500 to $+500 \text{ km s}^{-1}$ with a step of 1 km s^{-1} .

Before cross-correlation, we filtered the residual spectra using a Gaussian filter with a σ of $\sim 1.5 \text{ \AA}$. In this way, we filtered out large-scale spectral features, which could be caused by the blaze function variation and the stellar pulsation. We cross-correlated the residual spectra with the simulated template spectra as in Snellen et al. (2010). The cross-correlations of the Ca II H&K from HARPS-N observations and the Ca II IRT from

CARMENES observations were performed independently. For each observed spectrum, we obtained one cross-correlation function (CCF; Fig. 4b). We then combined all the in transit CCFs by shifting them to the planetary rest frame for a given K_p (RV semi-amplitude of planetary orbital motion). In this way, we generated the K_p -map with K_p ranging from 0 to 400 km s^{-1} with a step of 1 km s^{-1} (Fig. 4c). This two-dimensional CCF map has been widely used in previous cross-correlation studies, as in Fig. 8 of Birkby et al. (2017) and Fig. 14 of Nugroho et al. (2017). In order to estimate the S/N, we measured the noise of the K_p map as the standard deviation of CCF values with RV ranges of -200 to -100 km s^{-1} and $+100$ to $+200 \text{ km s}^{-1}$. Each K_p -map was then divided by the corresponding noise value.

4. Results and discussion

4.1. Detection of Ca II using the cross-correlation method

The cross-correlation results of the two planets are presented in Figs. 4 and 5. Panel b in the figures are cross-correlation maps between the model spectrum and the residual spectrum with the RM+CLV effects corrected. We also calculated the

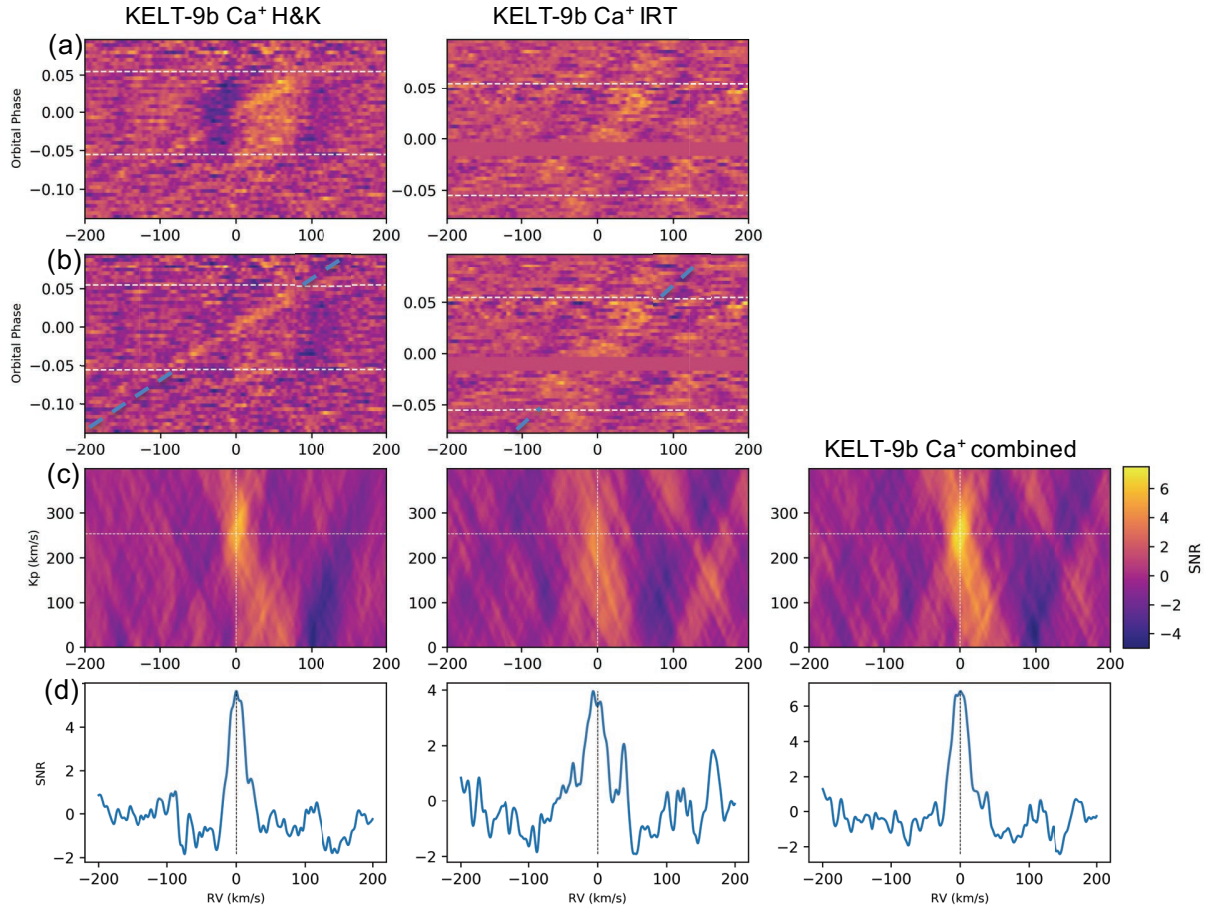


Fig. 5. Same as Fig. 4 but for KELT-9b. The expected K_p value for KELT-9b is 254 km s^{-1} .

cross-correlation maps between the model spectrum and the original residual spectrum for comparison (panel a).

The Ca II H&K and the Ca II IRT lines are detected from both planets. We further added the K_p -maps of H&K and IRT to obtain the combined K_p -map of the five Ca II lines (right panel in the figures). Here we directly added the H&K and IRT K_p -maps divided by their corresponding noise values. The combined K_p maps show strong cross-correlation signals at the expected K_p values ($231 \pm 3 \text{ km s}^{-1}$ for WASP-33b and $254^{+12}_{-10} \text{ km s}^{-1}$ for KELT-9b). These K_p values are calculated using Kepler's third law with orbital parameters from the literature (Tables 2 and 3). The peak S/N value in the K_p -map is located at $K_p = 224 \text{ km s}^{-1}$ for WASP-33b and $K_p = 266 \text{ km s}^{-1}$ for KELT-9b. For KELT-9b, Yan & Henning (2018) derived $K_p = 269 \pm 6 \text{ km s}^{-1}$ using H α absorption and Hoeijmakers et al. (2019) obtained a K_p value of $234.2 \pm 0.9 \text{ km s}^{-1}$ using the planetary Fe II absorption lines. These K_p values derived from planetary absorption are different, but broadly consistent, with the expected K_p values derived from orbital parameters. Considering that the planetary atmosphere may have additional RV components originated from dynamics, we decided to use the expected K_p values from Kepler's third law in the rest of the paper.

The bottom panel in the figures presents the CCFs at the expected K_p values. Since we already corrected for the systemic velocity as described in Sect. 3.1, the planetary signal is expected to be located at $RV \sim 0 \text{ km s}^{-1}$.

For WASP-33b, the Ca II IRT signal is very clear and can be seen in the CCF map directly (middle panel in Fig. 4b). The Ca II H&K signal is also strong but is less significant than the

IRT lines, probably because the deep stellar Ca II H&K lines significantly reduce the flux level. The combined cross-correlation function of the five lines yields a 11σ detection.

For KELT-9b, the CCF map of the Ca II H&K lines shows a clear signal. However, the Ca II IRT signal is less significant, which we attribute to the bad weather conditions during the CARMENES observation. Nevertheless, the IRT signal is still detected at a 4σ level as shown in Fig. 5d. The combined CCF shows a 7σ detection. The detection of Ca II IRT in KELT-9b was recently confirmed by Turner et al. (2019) during the review process of this paper.

The correction of the stellar RM and CLV effects plays an important role in the Ca II detection. By comparing the CCF maps with and without the stellar correction in Figs. 4 and 5, the improvement after the correction is significant. Hoeijmakers et al. (2019) searched for Ca II in KELT-9b using the same HARPS-N data as in this work, however they were not able to detect the Ca II H&K lines. Probably, the different treatment of the RM and CLV effects between our works could be responsible for the different results obtained. They used an empirical model to fit the stellar residuals presented in the CCF map, which did not properly correct the stellar RM and CLV effects of the H&K lines (see Fig. 3).

Stellar chromospheric activity can potentially affect the planetary Ca II detection but is not expected to pose a serious problem in early A-type stars (e.g., Schmitt 1997). Cauley et al. (2018) and Khalafinejad et al. (2018) investigated the effect of stellar activity on transmission spectra of calcium lines. One prominent distinction between stellar activity and planetary absorption is

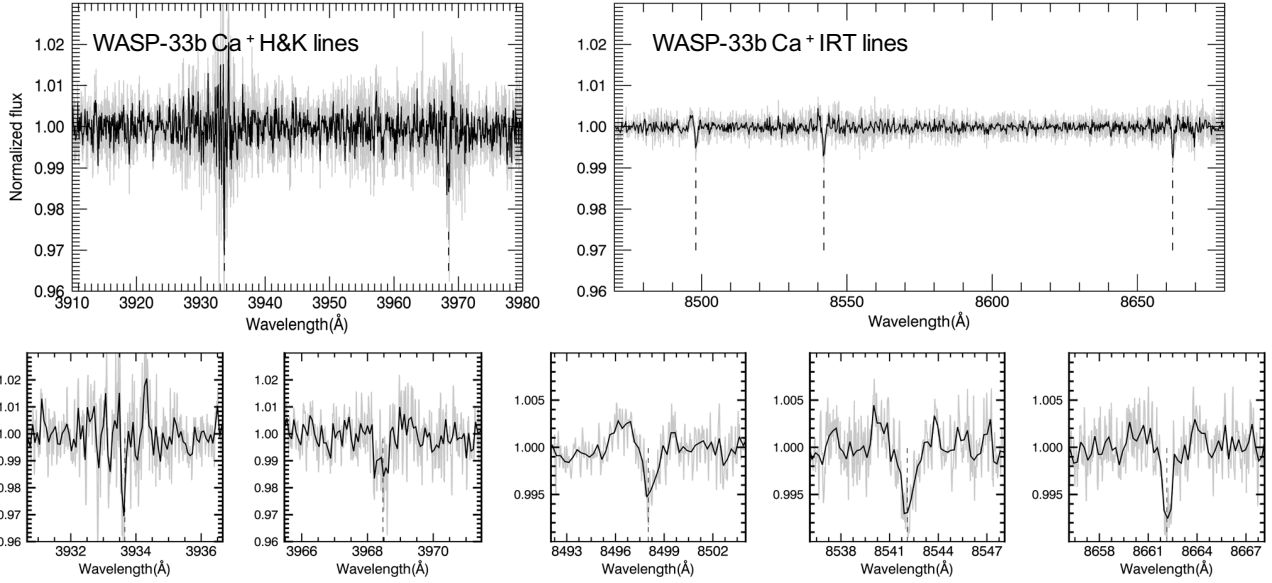


Fig. 6. Transmission spectra of the Ca II lines for WASP-33b obtained by combining all the in-transit spectra (excluding ingress and egress). Gray lines denote the original spectra and black lines the binned spectra (7 points bin). Dashed vertical lines indicate the rest wavelengths of the line centers. *Upper panels:* Ca II H&K and IRT lines plotted with the same y-axis scale. The strength of the H&K lines is significantly greater than that of the IRT lines. *Lower panels:* enlarged view of each of the five lines.

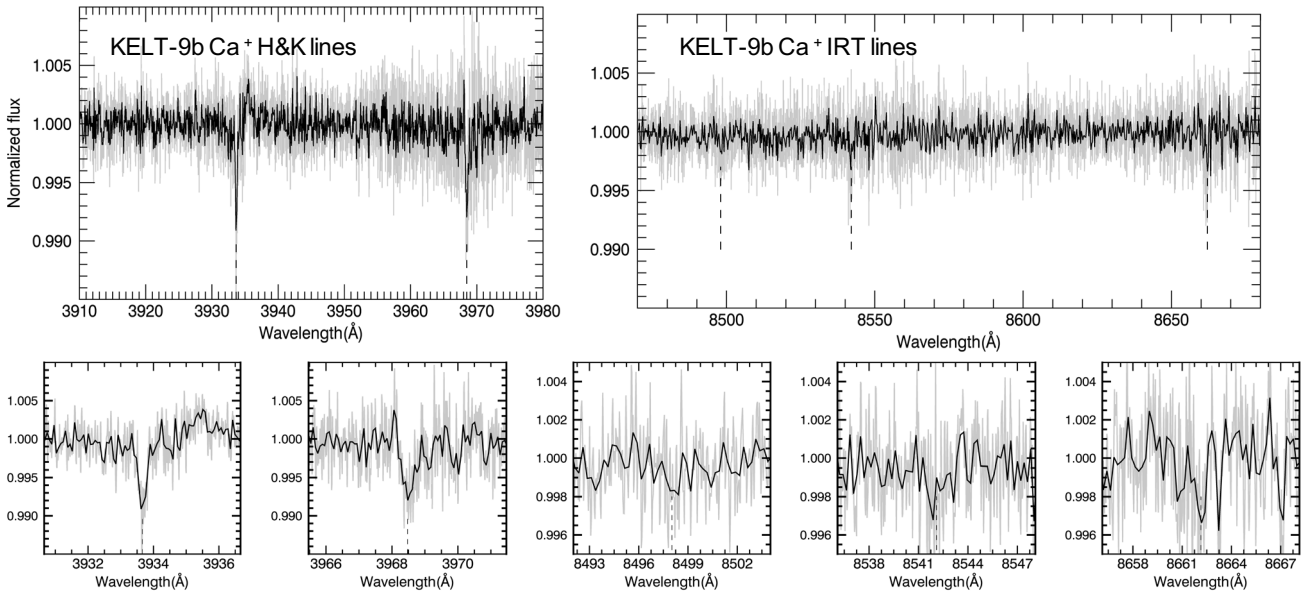


Fig. 7. Same as Fig. 6 but for KELT-9b.

the RV difference (Barnes et al. 2016). In our work, the detected Ca II signals follow the expected orbital velocities of KELT-9b and WASP-33b, which strongly support their planetary origin.

The host star of WASP-33b is a variable star and stellar pulsations could potentially change the stellar line profile (Collier Cameron et al. 2010). However, since the Ca II feature occurs at the planetary velocity and only during transit (cf. the middle figure in Fig. 4b), the detected signal is unlikely to be the result of stellar pulsation. Although the planetary atmosphere feature is unambiguous, the stellar pulsation features probably affect the CCF map. For instance, there is a feature in the IRT CCF map at around -30 km s^{-1} (see middle panel in Fig. 4b). Such a pulsation feature produces a dark region next to the planetary atmosphere signal on the K_p -map (middle panel in Fig. 4c).

4.2. Transmission spectrum of individual Ca II lines

In addition to the Ca II detection using the cross-correlation technique, we also obtained the transmission spectrum of each individual line in order to study them in detail (Figs. 6 and 7). We added up all the residual spectra observed in transit (but excluding the ingress and egress). Here the stellar RM and CLV effects are already corrected in the residual spectra. Before adding up, we shifted the spectra to the planetary rest frame using the literature K_p values.

In order to study the absorption line profile, we averaged the H&K lines as well as the triplet lines (see Fig. 8). We performed the averaging based on the fact that the line depths of the two H&K lines are similar and the line depths of the triplet lines are

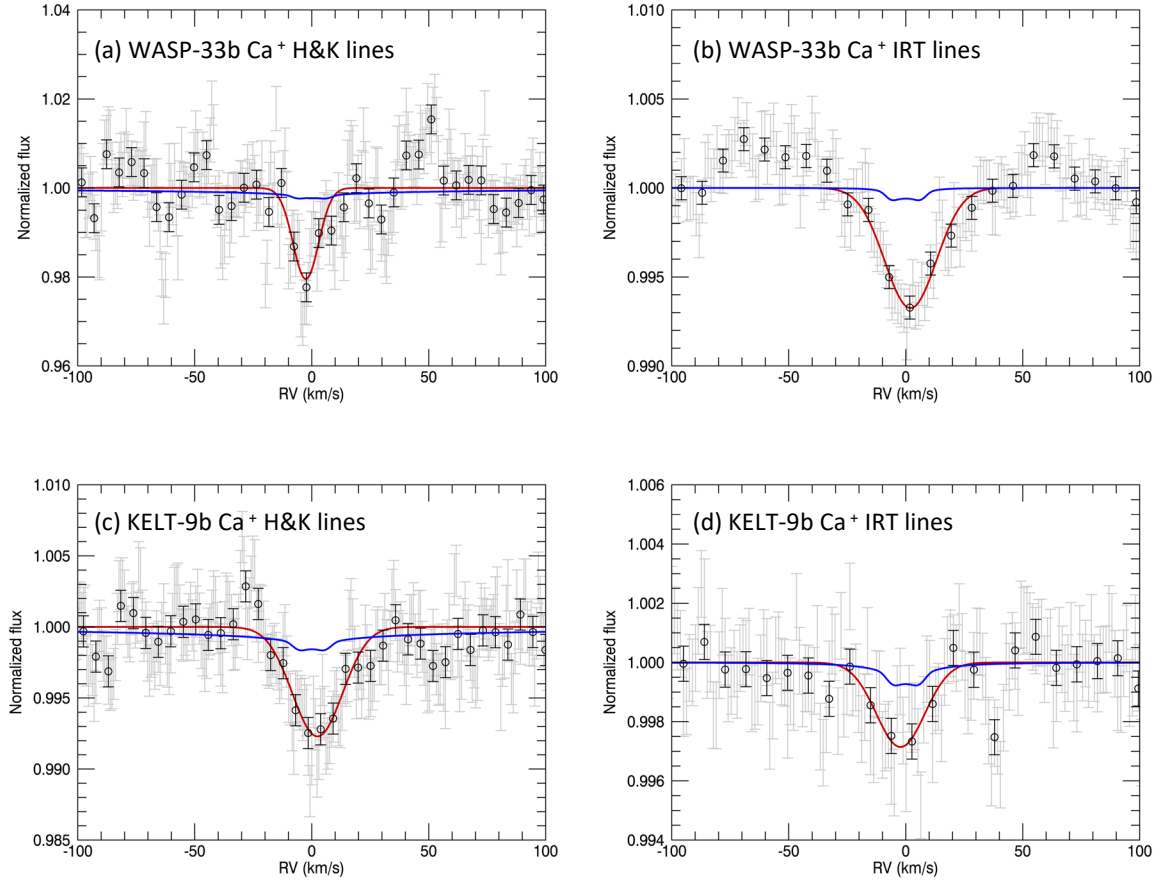


Fig. 8. Average line profiles of Ca II H&K (*left*) and Ca II IRT (*right*) for WASP-33b (*top*) and KELT-9b (*bottom*). The gray points are original transmission spectra and the black circles are spectra binned every seven points. The red lines are Gaussian fits to the line profiles. The fitted results are presented in Table 4. The blue lines are model spectra calculated assuming isothermal temperatures and tidally locked rotation.

Table 4. Line profile parameters obtained by fitting a Gaussian function to the average line profile in Fig. 8.

	Lines	v_{center} [km s ⁻¹]	$FWHM$ [km s ⁻¹]	Line depth	Model line depth	R_{eff} [R_p]
WASP-33b	Ca II H&K	-1.9 ± 0.7	15.2 ± 1.5	$(2.02 \pm 0.17)\%$	0.235%	1.56 ± 0.04
	Ca II IRT	2.0 ± 0.7	26.0 ± 1.7	$(0.67 \pm 0.04)\%$	0.064%	1.22 ± 0.01
KELT-9b	Ca II H&K	3.2 ± 0.7	27.5 ± 1.8	$(0.78 \pm 0.04)\%$	0.162%	1.47 ± 0.02
	Ca II IRT	-2.2 ± 2.2	24.4 ± 5.1	$(0.29 \pm 0.05)\%$	0.076%	1.19 ± 0.03

Notes. Here v_{center} is the measured RV shift of the line center compared to the theoretical line center. The model line depth is the average line depth from the Ca II transmission model. R_{eff} is the effective radius at the line center calculated using the observed line depth value and the photometric transit depth.

also similar. Subsequently, a Gaussian function is fitted to the average spectrum. The fit results are presented in Table 4. We measured the standard deviation of the spectrum in the ranges of -200 to -100 km s⁻¹ and $+100$ to $+200$ km s⁻¹ and assigned this value as the error of each data point.

The average line depth of the H&K lines is significantly greater than that of the IRT lines. The line depth ratio between them is 3.0 ± 0.3 for WASP-33b and 2.7 ± 0.5 for KELT-9b. This is because the H&K lines correspond to resonant transitions from the ground state of Ca II, while the IRT lines are not. For both planets, the 8542 Å line is the strongest and the 8498 Å line is the weakest among the three IRT lines. These relative line strengths are consistent with the transmission spectral model.

We calculated the effective radius at the line center (R_{eff}) and compared it with the effective Roche lobe radius at the planetary terminator (Ehrenreich 2010). Here, R_{eff} is obtained using the equation: $\pi R_{\text{eff}}^2 / \pi R_p^2 = (\delta + h) / \delta$, where δ is the optical photometric transit depth (cf. Tables 2 and 3) and h is the observed line depth. For WASP-33b, the R_{eff} of H&K lines is $1.56 R_p$ which is very close to the effective Roche radius ($1.71^{+0.08}_{-0.07} R_p$). For KELT-9b, the R_{eff} of H&K lines is $1.47 R_p$ and the effective Roche radius is $1.91^{+0.22}_{-0.26} R_p$. Therefore, the effective radii of both planets are close but below the Roche radii. As a result, we infer that the ionized calcium detected here mostly originates from the extended atmospheric envelope within the Roche lobe instead of from the already escaped material beyond the Roche lobe. Escaped material beyond the Roche lobe can potentially

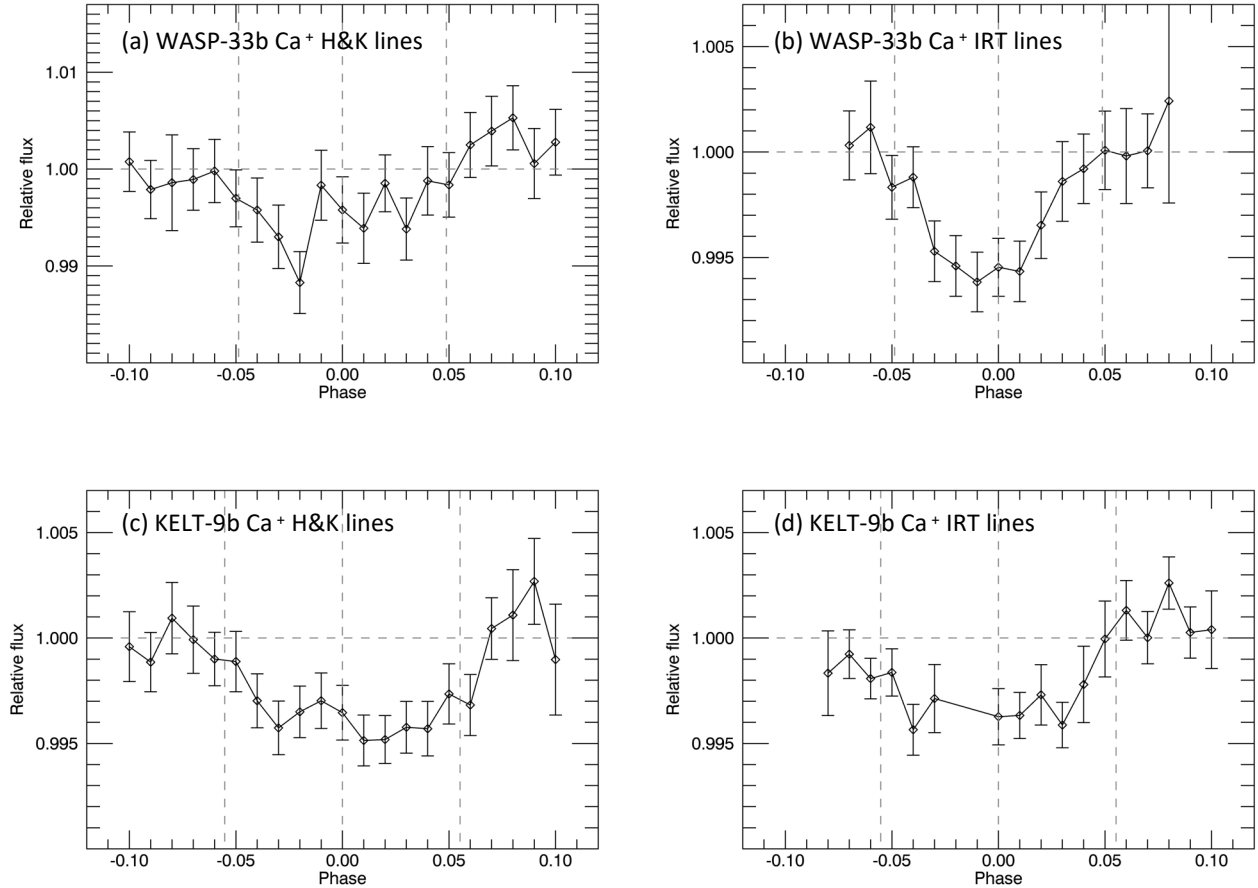


Fig. 9. Average light curves of the Ca II H&K lines (*left panels*) and Ca II IRT lines (*right panels*). These are relative fluxes measured with an 1 Å band centered at the line core. The measurement was performed in the planetary rest frame and the stellar RM+CLV effects were corrected.

form a comet-like tail as detected in some exoplanets using the hydrogen Lyman- α and the helium 1083 nm absorptions (e.g., Ehrenreich et al. 2015; Nortmann et al. 2018).

The full width at half maximum (FWHM) of the average line profile is also presented in Table 4. The FWHM values of the Ca II lines in KELT-9b agree in general with the values of other metal lines in KELT-9b measured by Cauley et al. (2019) and Hoeijmakers et al. (2019). The observed line width is probably a combined result of thermal broadening, rotational broadening, and hydrodynamic escape velocity.

The measured line centers have blue- or red-shifted RVs of several km s^{-1} (v_{center} values in Table 4). However, we do not claim the detection of atmospheric winds considering the large errors. The residuals of the RM and CLV effects as well as stellar pulsation can potentially affect the obtained transmission line profile. Furthermore, the uncertainty of the stellar systemic velocity also affects the measurement of v_{center} . For example, Gaudi et al. (2017) reported v_{sys} of KELT-9 to be $-20.6 \pm 0.1 \text{ km s}^{-1}$. However, Hoeijmakers et al. (2019) obtained a value of $-17.7 \pm 0.1 \text{ km s}^{-1}$ using HARPS-N observations. Later, Borsa et al. (2019) measured v_{sys} of KELT-9 as $-19.819 \pm 0.024 \text{ km s}^{-1}$ also using HARPS-N data. For WASP-33, Nugroho et al. (2017) found that their measured v_{sys} deviates from the values in other works by $\sim 1 \text{ km s}^{-1}$. The discrepancy between the v_{sys} measurements could be due to different instrument RV zero-points, stellar templates, and methods to measure RV, as well as to the relatively large stellar variability of WASP-33. In principle, RV measurement of fast rotating early-type stars like WASP-33 and

KELT-9 is intrinsically difficult because of the lack of sufficient stellar lines and the broad line profile. Therefore, one should be cautious when interpreting the measured shift of the line center as the signature of atmospheric winds.

In order to investigate the time series of the Ca II absorption, we measured the relative fluxes of each Ca II line in the residual spectra with an 1 Å band centered at the line core. Subsequently, we averaged the obtained light curves of the H&K lines and the IRT lines and binned the data points with a phase step of 0.01 (Fig. 9). The light curves of the WASP-33b IRT lines and the KELT-9b H&K lines have clear absorption signals during transit. However, the absorption signals are less prominent in the light curves of the WASP-33b H&K lines and the KELT-9b IRT lines, which is probably due to lower data quality, stellar pulsation noise, and residuals of the RM + CLV effects.

4.3. Mixing ratios of Ca I and Ca II

We calculated the equilibrium chemistry between atomic calcium (Ca I) and singly ionized calcium (Ca II) using the chemical module in the *petitCode* (Mollière et al. 2015, 2017). Figure 10 shows the mixing ratio variation with temperature. For an atmosphere with a solar metallicity and at a pressure of 10 mbar, ionized calcium becomes dominant at temperatures higher than 3000 K. In general, the calcium ionization rate is higher with higher temperature and lower pressure.

As calculated by Hoeijmakers et al. (2019), the spectral continuum level for UHJ is typically located between 1 mbar and

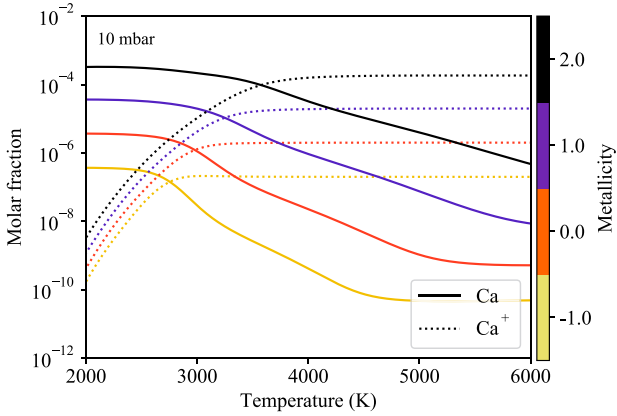


Fig. 10. The Ca I (solid line) and Ca II (dashed line) mixing ratios as a function of temperature. Here we assumed chemical equilibrium without photo-ionization and a pressure of 10 mbar. Different colors signify different metallicities ($[Fe/H]$ in unit of dex).

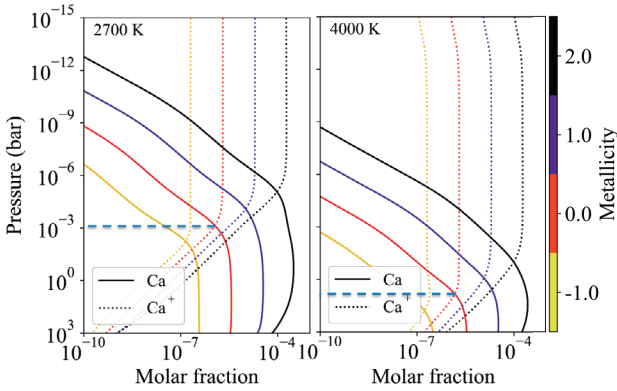


Fig. 11. Neutral and ionized calcium profiles for WASP-33b (left) and KELT-9b (right). Here we assumed isothermal temperatures as indicated in the top left corner of each panel. At solar metallicity (orange lines), Ca II is dominant at high altitudes with pressure <1 mbar for WASP-33b and with pressure <10 bar for KELT-9b (denoted with horizontal dashed lines).

10 mbar, and transmission spectroscopy probes only the atmosphere above the continuum level. Therefore, we expect Ca II to be the dominant calcium feature in the transmission spectroscopy of UHJs. The Ca I line can be probed at lower altitudes if the planetary atmosphere is cooler than 3000 K. For example, atomic calcium was detected in the relatively cool hot-Jupiter HD 209458b, which has a T_{eq} of 1460 K (Astudillo-Defru & Rojo 2013). Here we did not include photo-ionization in the chemical model. The ionization fraction will be higher when including photo-ionization.

Figure 11 shows the Ca I and Ca II mixing ratios of the two planets assuming isothermal temperature distributions. For WASP-33b, Ca II is dominant at high altitudes with pressures <1 mbar assuming solar metallicity; for KELT-9b, Ca II is dominant at pressures <10 bar. According to our simulations, the average H^- continuum level is located at ~ 8 mbar for WASP-33b and ~ 4 mbar for KELT-9b in the wavelength region studied here and assuming solar metallicity. Thus, for KELT-9b, Ca II is the dominant species in the region probed by transmission spectroscopy; for WASP-33b, Ca I can be probed at lower altitudes but only within a small altitude range from 1 mbar to ~ 8 mbar. We assumed isothermal temperature with T_{eq} values, but the actual temperature at the planetary terminators may deviate from

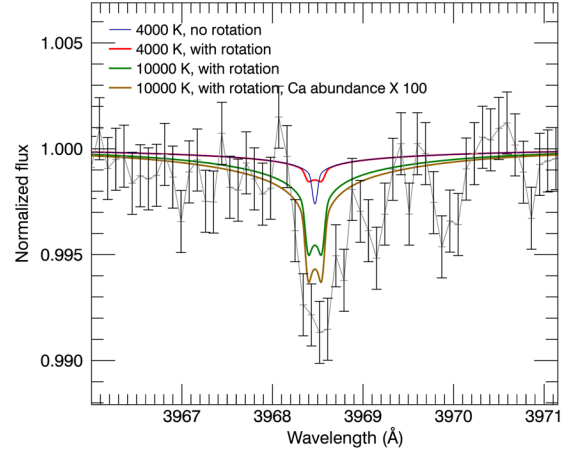


Fig. 12. Different models for the Ca II H line absorption for KELT-9b. The black points are the observed transmission spectrum (binned every 7 points). The blue line is the model with a temperature of 4000 K. The red line is the model with rotational broadening included. The green line is the model with a temperature of 10 000 K and the yellow line is with increased Ca abundance. The observed absorption is stronger than the model predictions. Such a strong absorption indicates a hydrodynamic outflow of the material.

T_{eq} depending on the 3D atmospheric circulation as well as other mechanisms such as temperature inversion. Therefore, the actual mixing ratio profiles could be different from those presented in Fig. 11.

We also searched for Ca I in the two planets using the cross-correlation method. Since most of the Ca I lines are in the HARPS-N wavelength region, we only cross-correlated the modeled Ca I spectrum with the HARPS-N dataset. The simulated stellar RM and CLV effects were corrected before the cross-correlation process. We were not able to detect Ca I signals in the two planets. Hoeijmakers et al. (2019) searched for Ca I in KELT-9b using two transit observations from HARPS-N and there was only tentative evidence of Ca I. These observational results imply that the atmospheres of the two planets are extremely hot and Ca II is dominant.

4.4. Model of Ca II transmission spectrum

The Ca II transmission spectra of both planets are significantly stronger than the model predictions that are calculated assuming equilibrium temperature and solar abundance (cf. Fig. 8). The second last column of Table 4 lists the line depths from the models. Here we considered the rotational broadening by assuming tidal locking using the method of Brogi et al. (2016). The observed line depths of WASP-33b are 8.6 and 10 times stronger than the depths from the model for the H&K and IRT lines, respectively. For KELT-9b, the observed line depths are 4.8 and 3.8 times stronger for the H&K and IRT lines, respectively. When increasing the isothermal temperature in the models, we obtained larger line depths because of the increased scale heights; the line depth also increases with an increasing calcium abundance. Figure 12 compares different models for the H line in KELT-9b. Even with temperature as high as 10 000 K and a Ca abundance 100 times the solar Ca abundance, the observed line depth is still stronger than the model.

When simulating the Ca II transmission spectrum, we set a cut-off level of 1 mbar to account for possible continuum opacities. The major continuum opacity for the two planets is H^- absorption. The H^- mixing ratio and the H^- transmission

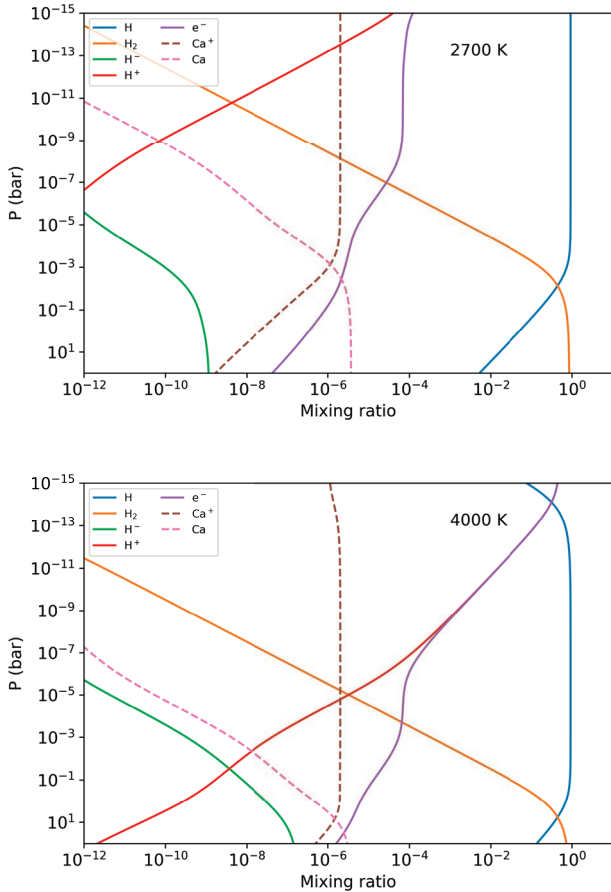


Fig. 13. Mixing ratios of hydrogen species calculated assuming solar metallicity, equilibrium chemistry, and isothermal temperature. The upper panel is for WASP-33b (2700 K) and the lower panel is for KELT-9b (4000 K). In both planets, H^- exists at low altitudes and is the main opacity source of the spectral continuum. The calcium profiles are also plotted as dashed lines.

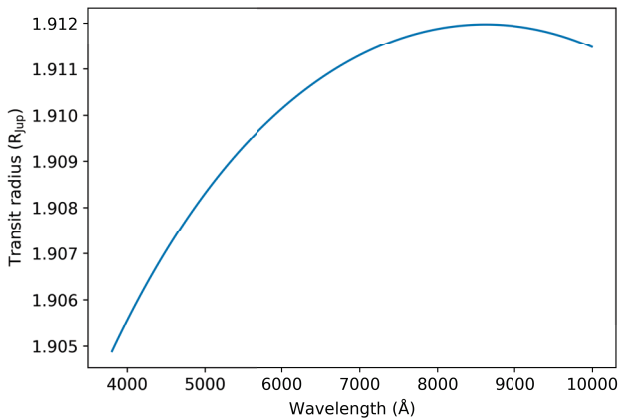


Fig. 14. Modeled transmission spectrum of H^- for KELT-9b.

spectrum are presented in Figs. 13 and 14, respectively. The absorption of H^- peaks at $\sim 0.85 \mu\text{m}$. The average H^- continuum level in the optical wavelength range is around 4 mbar and 8 mbar for KELT-9b and WASP-33b, respectively. In order to evaluate the impact of choosing different continuum levels, we simulated Ca II transmission spectra using cut-off levels from 0.1 mbar to 10 mbar and found that the line depth increased by less than 20%.

Therefore, we concluded that setting different continuum levels cannot explain the strong Ca II lines observed.

Such a strong Ca II absorption in the two planets can be caused by the hydrodynamic escape that brings up calcium ions, and as a result significantly enhances its density at high altitudes. Compared to hydrostatic models, the hydrodynamic outflow significantly increases the density of materials at altitudes close to the Roche lobe (Vidal-Madjar et al. 2004). Hoeijmakers et al. (2019) also found that the observed line depths are stronger than the modeled values and they attributed this discrepancy to the hydrodynamic escape that transports materials to high altitudes. Theoretical models predict that the atmospheres of UHJ are prone to strong atmospheric escape because they receive large amounts of stellar UV and/or extreme-UV radiation (Fossati et al. 2018). Yan & Henning (2018) observed a strong $\text{H}\alpha$ absorption in KELT-9b, which is evidence of substantial escape of the atmosphere. Further Ca II line modeling work with hydrodynamic escape included will be able to constrain the temperature profile and mass loss rate of the planets (e.g., Odert et al. 2019).

5. Conclusions

We detected singly ionized calcium in KELT-9b and WASP-33b – the two hottest hot-Jupiters discovered so far. Together with the very recent Ca II detection in MASCARA-2b, these three UHJs are the only exoplanets with Ca II detected in their atmospheres. Our Ca II detections and lack of Ca I detections demonstrate that calcium is probably mostly ionized into Ca II in the upper atmosphere of UHJs.

In addition to the detection using the cross-correlation method, we obtained the transmission spectra from the full set of the five Ca II lines (H&K doublet and near-infrared triplet). The effective radii of the H&K lines are close to the Roche lobes of the planets, indicating that the calcium ions are from the very upper atmospheres where mass loss is underway. The obtained line depths are significantly stronger than predictions by hydrostatic models assuming an isothermal temperature of T_{eq} . This is probably because the upper atmosphere is hotter than T_{eq} and hydrodynamic outflow brings up Ca II to the high altitudes. Further modeling work with hydrodynamic escape included is thought to be required to fit the line profile and retrieve the temperature structure.

Due to the high ionization rate of calcium in the upper atmospheres of UHJs and the strong opacities of the Ca II H&K and near-infrared triplet lines, the Ca II transmission spectrum is especially suitable for probing the high-altitude atmospheres and revealing the properties of this peculiar class of exoplanets. These lines have great potential for the study of planet-star interaction, such as atmospheric escape and the impact of stellar wind.

Acknowledgements. We are grateful to the anonymous referee for his/her report. F.Y. acknowledges the support of the DFG priority program SPP 1992 “Exploring the Diversity of Extrasolar Planets (RE 1664/16-1)”. CARMENES is an instrument for the Centro Astronómico Hispano-Alemán de Calar Alto (CAHA, Almería, Spain). CARMENES is funded by the German Max-Planck-Gesellschaft (MPG), the Spanish Consejo Superior de Investigaciones Científicas (CSIC), the European Union through FEDER/ERF FICTS-2011-02 funds, and the members of the CARMENES Consortium (Max-Planck-Institut für Astronomie, Instituto de Astrofísica de Andalucía, Landessternwarte Königstuhl, Institut de Ciències de l’Espai, Institut für Astrophysik Göttingen, Universidad Complutense de Madrid, Thüringer Landessternwarte Tautenburg, Instituto de Astrofísica de Canarias, Hamburger Sternwarte, Centro de Astrobiología and Centro Astronómico Hispano-Alemán), with additional contributions by the Spanish Ministry of Economy, the German Science Foundation through the

Major Research Instrumentation Programme and DFG Research Unit FOR2544 “Blue Planets around Red Stars”, the Klaus Tschira Stiftung, the states of Baden-Württemberg and Niedersachsen, and by the Junta de Andalucía. Based on data from the CARMENES data archive at CAB (INTA-CSIC). This work is based on observations made with the Italian Telescopio Nazionale *Galileo* (TNG) operated on the island of La Palma by the Fundación Galileo Galilei of the INAF (Istituto Nazionale di Astrofisica) at the Spanish Observatorio del Roque de los Muchachos of the Instituto de Astrofísica de Canarias. P.M. and I.S. acknowledge support from the European 82 Research Council under the European Union’s Horizon 2020 research and innovation program under grant agreement No. 694513.

References

- Alonso-Floriano, F. J., Sánchez-López, A., Snellen, I. A. G., et al. 2019, *A&A*, **621**, A74
- Arcangeli, J., Désert, J.-M., Line, M. R., et al. 2018, *ApJ*, **855**, L30
- Astudillo-Defru, N., & Rojo, P. 2013, *A&A*, **557**, A56
- Barnes, J. R., Haswell, C. A., Staab, D., & Anglada-Escudé, G. 2016, *MNRAS*, **462**, 1012
- Bell, T. J., & Cowan, N. B. 2018, *ApJ*, **857**, L20
- Birkby, J. L., de Kok, R. J., Brogi, M., Schwarz, H., & Snellen, I. A. G. 2017, *AJ*, **153**, 138
- Bisikalo, D., Kaygorodov, P., Ionov, D., et al. 2013, *ApJ*, **764**, 19
- Borsa, F., Rainer, M., Bonomo, A. S., et al. 2019, *A&A*, **631**, A34
- Brogi, M., de Kok, R. J., Albrecht, S., et al. 2016, *ApJ*, **817**, 106
- Caballero, J. A., Guàrdia, J., López del Fresno, M., et al. 2016, *Proc. SPIE*, **9910**, 99100E
- Casasayas-Barris, N., Pallé, E., Yan, F., et al. 2018, *A&A*, **616**, A151
- Casasayas-Barris, N., Pallé, E., Yan, F., et al. 2019, *A&A*, **628**, A9
- Cauley, P. W., Kuckein, C., Redfield, S., et al. 2018, *AJ*, **156**, 189
- Cauley, P. W., Shkolnik, E. L., Ilyin, I., et al. 2019, *AJ*, **157**, 69
- Collier Cameron, A., Guenther, E., Smalley, B., et al. 2010, *MNRAS*, **407**, 507
- Czesla, S., Klocová, T., Khalafinejad, S., Wolter, U., & Schmitt, J. H. M. M. 2015, *A&A*, **582**, A51
- Ehrenreich, D. 2010, *EAS Pub. Ser.*, **41**, 429
- Ehrenreich, D., Bourrier, V., Wheatley, P. J., et al. 2015, *Nature*, **522**, 459
- Foreman-Mackey, D., Hogg, D. W., Lang, D., & Goodman, J. 2013, *PASP*, **125**, 306
- Fossati, L., Haswell, C. A., Froning, C. S., et al. 2010, *ApJ*, **714**, L222
- Fossati, L., Koskinen, T., Lothringer, J. D., et al. 2018, *ApJ*, **868**, L30
- Gaudi, B. S., Stassun, K. G., Collins, K. A., et al. 2017, *Nature*, **546**, 514
- Guenther, E. W., Cabrera, J., Erikson, A., et al. 2011, *A&A*, **525**, A24
- Haynes, K., Mandell, A. M., Madhusudhan, N., Deming, D., & Knutson, H. 2015, *ApJ*, **806**, 146
- Helling, C., Gourbin, P., Woitke, P., & Parmentier, V. 2019, *A&A*, **626**, A133
- Herrero, E., Morales, J. C., Ribas, I., & Naves, R. 2011, *A&A*, **526**, L10
- Hoeijmakers, H. J., Ehrenreich, D., Heng, K., et al. 2018, *Nature*, **560**, 453
- Hoeijmakers, H. J., Ehrenreich, D., Kitzmann, D., et al. 2019, *A&A*, **627**, A165
- Jensen, A. G., Cauley, P. W., Redfield, S., Cochran, W. D., & Endl, M. 2018, *AJ*, **156**, 154
- Johnson, M. C., Cochran, W. D., Collier Cameron, A., & Bayliss, D. 2015, *ApJ*, **810**, L23
- Keles, E., Mallonn, M., von Essen, C., et al. 2019, *MNRAS*, **489**, L37
- Khalafinejad, S., Salz, M., Cubillos, P. E., et al. 2018, *A&A*, **618**, A98
- Kovács, G., Kovács, T., Hartman, J. D., et al. 2013, *A&A*, **553**, A44
- Kreidberg, L., Line, M. R., Parmentier, V., et al. 2018, *AJ*, **156**, 17
- Lehmann, H., Guenther, E., Sebastian, D., et al. 2015, *A&A*, **578**, L4
- Lothringer, J. D., Barman, T., & Koskinen, T. 2018, *ApJ*, **866**, 27
- Maciejewski, G., Fernández, M., Aceituno, F., et al. 2018, *Acta Astron.*, **68**, 371
- McLaughlin, D. B. 1924, *ApJ*, **60**, 22
- Mollière, P., van Boekel, R., Dullemond, C., Henning, T., & Mordasini, C. 2015, *ApJ*, **813**, 47
- Mollière, P., van Boekel, R., Bouwman, J., et al. 2017, *A&A*, **600**, A10
- Mollière, P., Wardenier, J. P., van Boekel, R., et al. 2019, *A&A*, **627**, A67
- Mura, A., Wurz, P., Schneider, J., et al. 2011, *Icarus*, **211**, 1
- Nortmann, L., Pallé, E., Salz, M., et al. 2018, *Science*, **362**, 1388
- Nugroho, S. K., Kawahara, H., Masuda, K., et al. 2017, *AJ*, **154**, 221
- Odert, P., Erkaev, N. V., Kislyakova, K. G., et al. 2019, *A&A*, submitted [arXiv:1903.10772]
- Parmentier, V., Line, M. R., Bean, J. L., et al. 2018, *A&A*, **617**, A110
- Queloz, D., Eggenberger, A., Mayor, M., et al. 2000, *A&A*, **359**, L13
- Quirrenbach, A., Amado, P. J., Ribas, I., et al. 2018, *Proc. SPIE Conf. Ser.*, **10702**, 107020W
- Ridden-Harper, A. R., Snellen, I. A. G., Keller, C. U., et al. 2016, *A&A*, **593**, A129
- Rossiter, R. A. 1924, *ApJ*, **60**, 15
- Salz, M., Czesla, S., Schneider, P. C., et al. 2018, *A&A*, **620**, A97
- Schmitt, J. H. M. M. 1997, *A&A*, **318**, 215
- Snellen, I. A. G., de Kok, R. J., de Mooij, E. J. W., & Albrecht, S. 2010, *Nature*, **465**, 1049
- Turner, J. D., de Mooij, E. J. W., Jayawardhana, R., et al. 2019, *ApJ*, submitted [arXiv:1910.06882]
- Vervack, R. J., McClintock, W. E., Killen, R. M., et al. 2010, *Science*, **329**, 672
- Vidal-Madjar, A., Désert, J. M., Lecavelier des Etangs, A., et al. 2004, *ApJ*, **604**, L69
- von Essen, C., Czesla, S., Wolter, U., et al. 2014, *A&A*, **561**, A48
- von Essen, C., Mallonn, M., Welbanks, L., et al. 2019, *A&A*, **622**, A71
- Wytenbach, A., Ehrenreich, D., Lovis, C., Udry, S., & Pepe, F. 2015, *A&A*, **577**, A62
- Yan, F., & Henning, T. 2018, *Nat. Astron.*, **2**, 714
- Yan, F., Fosbury, R. A. E., Petr-Gotzens, M. G., Zhao, G., & Pallé, E. 2015a, *A&A*, **574**, A94
- Yan, F., Fosbury, R. A. E., Petr-Gotzens, M. G., et al. 2015b, *Int. J. Astrobiol.*, **14**, 255
- Yan, F., Pallé, E., Fosbury, R. A. E., Petr-Gotzens, M. G., & Henning, T. 2017, *A&A*, **603**, A73